Intrinsic glassy-metallic transport in an amorphous coordination polymer

https://doi.org/10.1038/s41586-022-05261-4

Received: 20 January 2022

Accepted: 22 August 2022

Published online: 26 October 2022

Check for updates

Jiaze Xie¹, Simon Ewing^{1,2}, Jan-Niklas Boyn^{1,2}, Alexander S. Filatov¹, Baorui Cheng¹, Tengzhou Ma3, Garrett L. Grocke3, Norman Zhao1, Ram Itani1, Xiaotong Sun4, Himchan Cho1.5, Zhihengyu Chen⁶, Karena W. Chapman⁶, Shrayesh N. Patel³, Dmitri V. Talapin^{1,2,3,7}, Jiwoong Park^{1,2,3}, David A. Mazziotti^{1,2} & John S. Anderson^{1⊠}

Conducting organic materials, such as doped organic polymers¹, molecular conductors^{2,3} and emerging coordination polymers⁴, underpin technologies ranging from displays to flexible electronics⁵. Realizing high electrical conductivity in traditionally insulating organic materials necessitates tuning their electronic structure through chemical doping⁶. Furthermore, even organic materials that are intrinsically conductive, such as single-component molecular conductors^{7,8}, require crystallinity for metallic behaviour. However, conducting polymers are often amorphous to aid durability and processability⁹. Using molecular design to produce high conductivity in undoped amorphous materials would enable tunable and robust conductivity in many applications¹⁰, but there are no intrinsically conducting organic materials that maintain high conductivity when disordered. Here we report an amorphous coordination polymer, Ni tetrathiafulvalene tetrathiolate, which displays markedly high electronic conductivity (up to 1,200 S cm⁻¹) and intrinsic glassymetallic behaviour. Theory shows that these properties are enabled by molecular overlap that is robust to structural perturbations. This unusual set of features results in high conductivity that is stable to humid air for weeks, pH 0-14 and temperatures up to 140 °C. These findings demonstrate that molecular design can enable metallic conductivity even in heavily disordered materials, raising fundamental questions about how metallic transport can exist without periodic structure and indicating exciting new applications for these materials.

Using molecular design to engender high conductivity in undoped amorphous materials would enable tunable and robust conductivity in many applications, but there are no intrinsically conducting organic materials that maintain high conductivity when completely disordered. Inorganic glassy metals have been discovered but require careful fabrication¹¹. Furthermore, the relationship between metallic behaviour, which classically requires periodicity giving rise to a well-defined band structure, and geometric disorder in glassy metals is still unclear¹². Electron-rich and redox-active tetrathiafulvalene (TTF) motifs feature prominently as molecular building blocks in conducting materials8. Appending thiolate groups to TTF to generate tetrathiafulvalene tetrathiolate (TTFtt) enables the formation of extended coordination polymers that combine TTF motifs with electronically complex $transition\ metal\ dithiolenes^{13}.\ Although\ the\ promise\ of\ these\ materials$ has been recognized, their structure, purity, composition and hence properties are not well-defined because of synthetic challenges14.

We recently discovered syntheses for a series of redox congeners of capped TTFtt compounds and their facile transmetalation to group 10 metals¹⁵. Here we report that this synthetic strategy enables the isolation of the material NiTTFtt in high purity as an amorphous powder. Despite its disordered structure. NiTTFtt exhibits notable conductivity. as high as 1,200 S cm⁻¹ at room temperature, and glassy-metallic electronic behaviour. Theory shows that these properties are enabled by strong molecular overlap that is robust to structural perturbations. This unusual set of structural and electronic features results in conductivity that is robust to air, water, acid/base and temperatures up to 140 °C. These results demonstrate that molecular design can enable metallic conductivity even in completely disordered materials, raising fundamental questions about charge transport mechanisms in disordered materials and indicating exciting new applications for intrinsically metallic organic materials.

Synthesis and structure

NiTTFtt is synthesized by mixing [TTFtt(SnBu₂)₂][BAr₄^F]₂(BAr₄^F = tetrakis (3,5-bis(trifluoromethyl)phenyl)borate, Bu = n-butyl) with excess [TEA]₂[NiCl₄] (Fig. 1a; TEA, tetraethylammonium). Composition analyses support a Ni:S ratio of 1:8 and confirm the proposed formula of NiTTFtt with [Bu₂Sn][BAr^F] chain terminations (Supplementary Tables 5 and 6). The absence of ammonium counterions implies that the TTF

Department of Chemistry, University of Chicago, Chicago, Chicago, Illinois, USA. 2 James Franck Institute, University of Chicago, Chicago, Illinois, USA. 3 Pritzker School of Molecular Engineering University of Chicago, Chicago, Illinois, USA, Department of Human Genetics, University of Chicago, Chicago, Illinois, USA, Department of Materials Science and Engineering, Korea Advanced Institute of Science and Technology, Dajeon, South Korea. Department of Chemistry, Stony Brook University, Stony Brook, New York, USA. Center for Nanoscale Materials, Argonne National Laboratory, Argonne, IL, USA. [™]e-mail: jsanderson@uchicago.edu

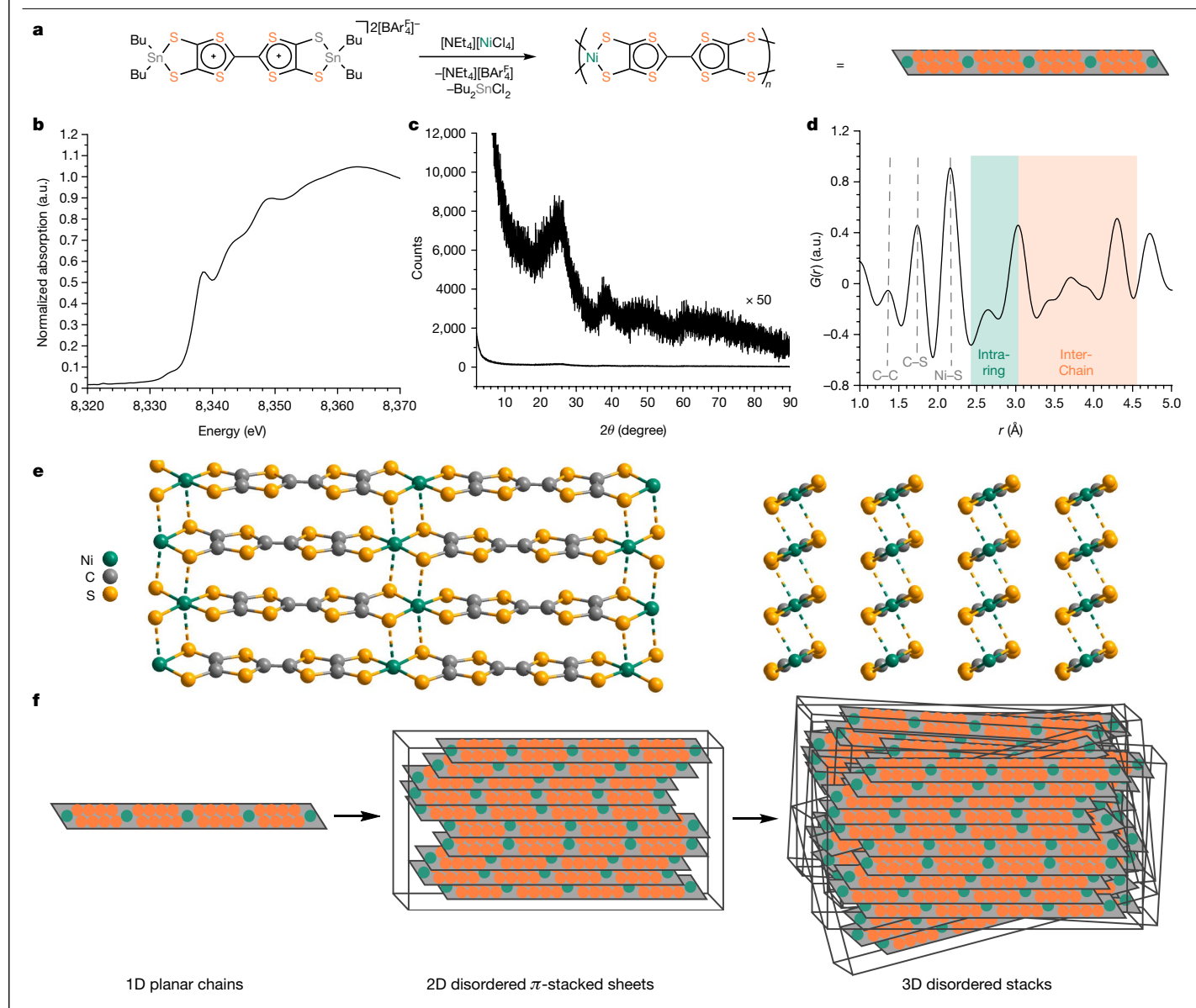


Fig. 1 | **Synthesis and structure of NiTTFtt. a**, Synthetic scheme. **b**, Ni K-edge X-ray absorption near-edge structure spectrum of amorphous NiTTFtt powder. **c**, PXRD pattern of amorphous NiTTFtt powder. **d**, Pair distribution function of amorphous NiTTFtt powder. **e**, Proposed idealized structure based on

structural characterization of semicrystalline NiTTFtt. ${\bf f}$, Hierarchical structure showing coplanar chains but disordered packing in sheets and stacks.

cores have formal 2+ charges, which is also supported by the absence of electron paramagnetic resonance (EPR) signals⁸ (Supplementary Fig. 44). X-ray photoelectron spectroscopy (Supplementary Fig. 24) reveals features at 871 and 854 eV, assigned as Ni $2p_{1/2}$ and $2p_{3/2}$ peaks respectively, and a satellite at 860 eV associated with a plasmon loss, all of which are consistent with low-spin (S=0) square planar Ni(II) centres. The S 2p spectra appear with a head and shoulder pattern spanning 161-166 eV, indicating multiple sulfur sites in NiTTFtt, and are similar to spectra of TTF[Ni(dmit)₂] (dmit, 1,3-dithole-2-thione-4,5-dithiolate)¹⁶. Ni K-edge X-ray absorption spectroscopy shows a rising edge at 8,338.6(4) eV, which also supports the assignment of pseudo- D_{4h} Ni(II) centres (Fig. 1b)¹⁷.

There are only broad features in the powder X-ray diffraction (PXRD) pattern for NiTTFtt, which indicate an amorphous material with domain sizes of around 1 nm, similar to amorphous silica 18 (Fig. 1c and Supplementary Fig. 8). Variable-temperature X-ray scattering and differential scanning calorimetry confirm that this amorphous structure persists from -90 to $210\,^{\circ}\mathrm{C}$ with no phase changes (Supplementary Figs. 10 and 63).

We have also investigated the structure of NiTTFtt with X-ray pair distribution function (PDF) analysis (Fig. 1d). The peaks below 3 Å can be assigned to C-C, C-S and Ni-S bonds, and intraring distances. The peaks between 3 and 4.5 Å represent additional interchain distances and are consistent with typical intermolecular S-S distances in TTF systems⁸.

Despite the amorphous nature of NiTTFtt, we have built a structural model based on experimental data (Fig. 1e). This model is supported by attempts to grow more crystalline NiTTFtt by slow diffusion, which show a PXRD pattern that can be indexed to a monoclinic unit cell (Supplementary Figs. 9 and 21). This unit cell indicates staggered coplanar chain packings with S–S distances of around 3.4–3.7 Å along the π -stack and around 3 and 4 Å side-to-side between chains. These values are similar to those observed in the single-component molecular metal, Ni(tmdt) $_2$ (tmdt, trimethylene-tetrathiafulvalene-dithiolate) 19 , and also support tight packing as previously proposed 20 . This model indicates that the disordered structure of NiTTFtt arises from one-dimensional (1D) chains that pack face-to-face into disordered two-dimensional

Table 1 | Summary of electronic, thermal, magnetic and optical properties

Physical properties	NiTTFtt
Electrical conductivity (Scm ⁻¹)	470-1,200
Thermal conductivity (W m ⁻¹ K ⁻¹)	6.3(1)
Lorenz number (WΩK ⁻²)	1.7×10 ⁻⁷
Arrhenius fit, E_a (meV)	0.08-2.1
Mott 3D VRH fit, T_0 (K)	13
Efros–Shklovskii fit, T_{ES} (K)	1.4
Seebeck coefficient (µV K ⁻¹)	-3.6(1)
Pauli paramagnetic susceptibility, χ _{Pauli} (cm ³ mol ⁻¹)	6.0×10 ⁻⁴
Plasma frequency (cm ⁻¹)	~12,000
Carrier concentration (cm ⁻¹)	~10 ²¹

(2D) sheets that then pack side-to-side into a three-dimensional (3D) structure (Fig. 1f). Scanning electron microscopy (SEM) confirms the presence of 2D flakes (Supplementary Figs. 19 and 20). Importantly, this structure mandates planar NiTTFtt chains that can π -stack strongly; both features should facilitate electronic delocalization.

Physical properties

Four-probe conductivity measurements on pressed pellets of NiTTFtt at room temperature reveal a conductivity of 470 ± 30 S cm⁻¹. Pellets hot-pressed at 200 °C provide values as high as 1,200 S cm⁻¹ (Table 1 and Supplementary Fig. 48). These values make NiTTFtt among the most conductive organic materials. The thermal conductivity of NiTTFtt was measured by Raman thermometry as 6.3(1) W m⁻¹ K⁻¹ (ref. ²¹; Supplementary Fig. 51), a value similar to inorganic glassy metals²², but higher than typical coordination polymers (lower

than 0.4 W m⁻¹K⁻¹)²³. The resulting Lorentz number at 300 K, 1.7×10^{-7} W Ω K⁻², is roughly one order magnitude higher than that for most metals, 2.44×10^{-8} W Ω K⁻². This deviation may arise from limited measurement accuracy but may also be related to weak localization as seen in molecular conductors²⁴.

Variable-temperature conductivity experiments on pressed pellets of amorphous NiTTFtt show an almost temperature-independent electrical resistivity with only a slight increase at low temperatures (Fig. 2a). Arrhenius fitting gives an activation energy of 2.1 meV above 60 K and 0.08 meV below 20 K (Supplementary Fig. 54). These extremely small barriers may arise for two reasons. Macroscopic interparticle transport may provide a barrier to charge flow as is frequently observed in pressed pellets of conducting organic materials^{7,25}. Alternatively, a flat variable-temperature conductivity profile has been observed for glassy metals with resistivities greater than 150 $\mu\Omega$ cm (ref. ²⁶). The increase of resistivity as temperature (*T*) decreases has been ascribed to 'weak localization' with a characteristic $T^{1/2}$ upturn in resistivity due to electron-electron interactions. We observe this same $T^{1/2}$ dependence at low temperature, indicating similar behaviour in NiTTFtt. This observation, combined with a finite zero-temperature extrapolation of the resistivity, indicates that NiTTFtt is best thought of as having metallic character²⁶.

Charge transport in disordered systems is typically analysed with variable-range hopping (VRH) models. Application of a 3D Mott VRH model to the resistivity data of NiTTFtt gives $T_0 = 13$ K, which indicates a high density of states at the Fermi level (Supplementary Fig. 55). Ultraviolet photoelectron spectroscopy of a pellet of NiTTFtt also supports a non-zero density of states at the Fermi level (Fig. 2b). Values of T_0 between 1 and 10⁴ K are commonly observed in granular metals in which hopping between metallic islands is assumed²⁷. The observed $T^{1/2}$ upturn in resistivity led us to apply the Efros-Shklovskii VRH model in this region (Supplementary Fig. 56). The observed linear relation $ship\ indicates\ the\ presence\ of\ a\ Coulomb\ gap,\ which\ further\ indicates$ electron-electron interactions as discussed above. Interestingly, the T_{ES} value obtained from this fit is extremely small, 1.4 K, indicating

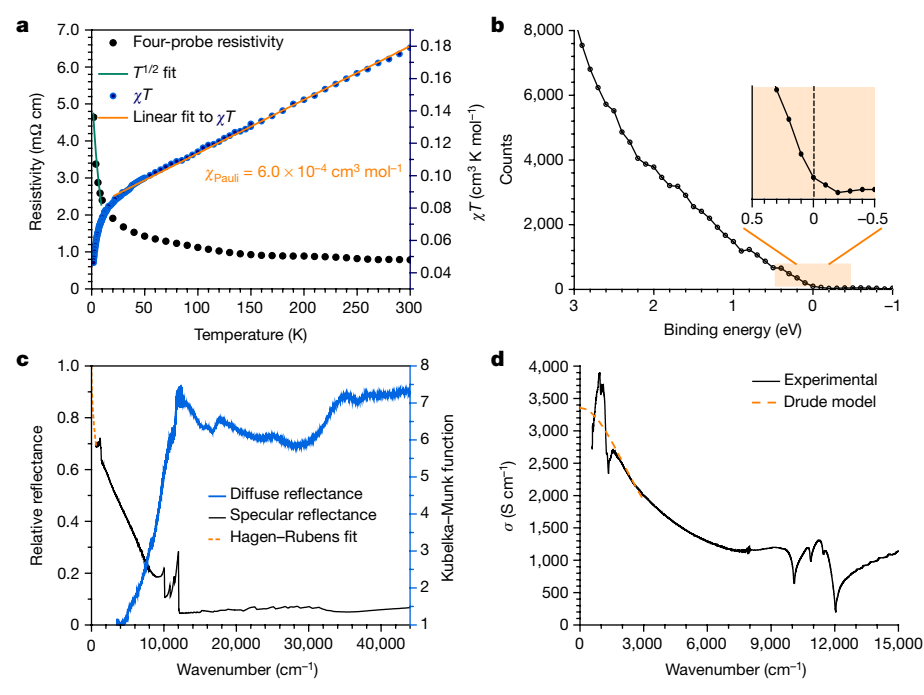


Fig. 2 | Physical properties of amorphous NiTTFtt. a, Variable-temperature resistivity (black) and magnetic susceptibility (blue) data. The green line indicates a $T^{1/2}$ fit to the resistivity data at low temperature accounting for weak localization and the orange line indicates a linear fit to the magnetic susceptibility data with the shown Pauli paramagnetic contribution.

b, Ultraviolet photoelectron spectrum showing a non-zero density of states at the Fermi level. c, Specular (black) and diffuse (blue) reflectance data. A Hagen-Rubens fit at low energy is shown by an orange dashed line (see Supplementary Fig. 59 for an enlarged view). **d**, Optical conductivity at the low energy limit with a Drude model fit shown by an orange dashed line.

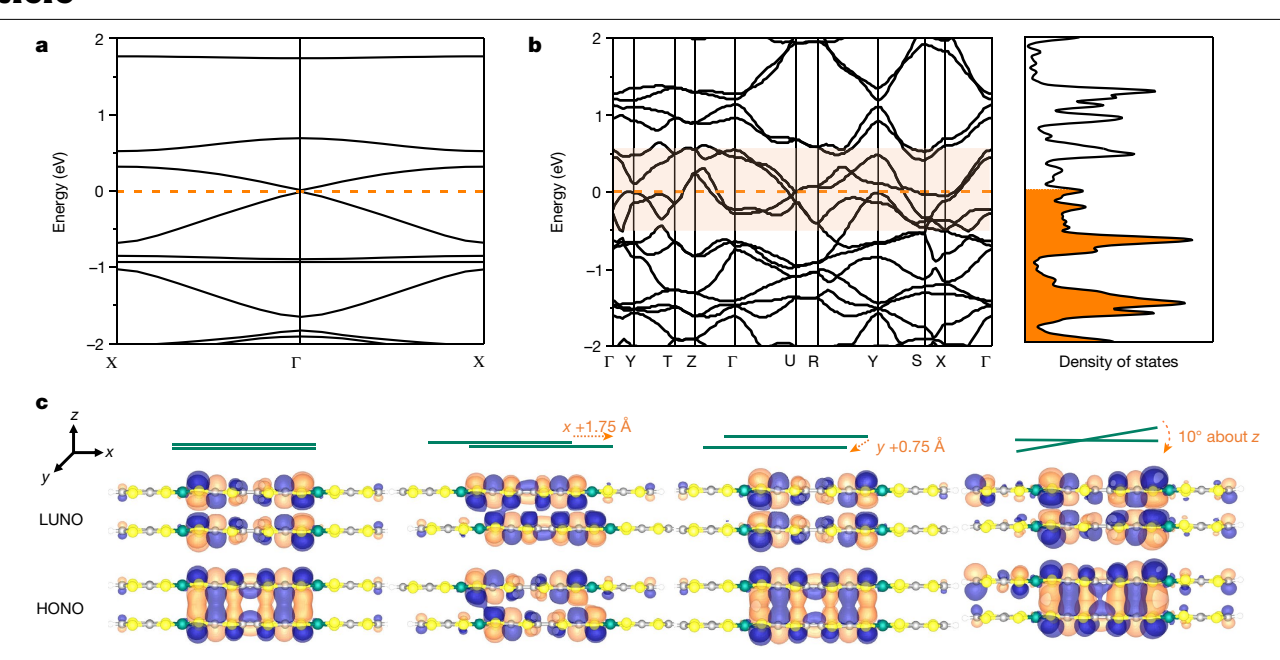


Fig. 3 | **Theoretical analysis of NiTTFtt. a**, Computed band structure of an isolated chain. **b**, Computed band structure of the idealized 3D structure determined from experimental data. **c**, Orbital diagrams of a molecular dimer

of NiTTFtt building blocks showing that substantial overlap is maintained regardless of structural distortions. HONO, highest occupied natural orbital; LUNO, lowest unoccupied natural orbital.

large delocalization lengths $^{28}\!$. All these data support glassy-metallic conductivity in NiTTFtt.

The Seebeck coefficient of NiTTFtt is $-3.6(1) \, \mu V \, K^{-1}$ and its magnitude increases linearly with temperature (Supplementary Fig. 57). The negative Seebeck coefficient indicates that electrons are the charge carriers and the small magnitude and linearity with temperature are commonly observed in metallic inorganic conductors²⁹. The magnetic susceptibility, χ , of NiTTFtt is only weakly temperature dependent, implying a paramagnetic contribution from charge carriers, namely Pauli paramagnetism (Fig. 2a). The value of χ_{Pauli} , $6 \times 10^{-4} \, \text{cm}^3 \, \text{mol}^{-1}$, is consistent with reported values in organic metals⁷⁸. Finally, we note a deviation from linearity in χT at low temperatures, which coincides with the increase in resistivity and putative weak localization.

We wanted to obtain more detailed quantification of the metallic nature of NiTTFtt and so we used both diffuse and specular reflectance spectroscopies 30,31 (Fig. 2c). NiTTFtt has a broad absorption over the ultraviolet (UV)–visible (vis)–near-infrared (NIR) region up to around 12,000 cm $^{-1}$. At the low frequency limit, the Hagen–Rubens relation can be used to extrapolate the specular reflectance to zero frequency and thereby estimate the d.c. conductivity as approximately 4,200 S cm $^{-1}$, a value which is consistent with four-probe measurements on pressed pellets (1,200 S cm $^{-1}$). The observed plasma frequency of approximately 12,000 cm $^{-1}$ provides a carrier density of $10^{21}\,\mathrm{cm}^{-3}$, which is similar to values in crystalline metallic polymers 1,26 .

We have further analysed the reflectivity data by applying the Kramers–Kronig transformation (Fig. 2d). Surprisingly, the optical conductivity from this analysis continuously increases as the frequency goes to zero. This behaviour, particularly in the far-IR region below 3,000 cm⁻¹, is suggestive of Drude behaviour for a classic metal³². Although the data range and quality limit fitting reliability, analysis of these data with a Drude model ($\sigma_{\rm D}(\omega) = (\omega_{\rm p}^2 \tau/4\pi)(1+\omega^2\tau^2)$; ω , wavenumber) gives a plasma frequency ($\omega_{\rm p}$) of 12,000 cm⁻¹, a relaxation time (τ) of 9.0 × 10⁻¹⁵ s, a d.c. conductivity of 3,300 S cm⁻¹, a carrier density of 3.4 × 10²¹ cm⁻³ (assuming effective mass $m^* = 2m_{\rm e}$)³², and a mean free path of around 2.4 nm (Supplementary Information). Thus, all fitted and measured values for NiTTFtt across different techniques are consistent and support metallic behaviour. The Drude-like behaviour and small $T_{\rm ES}$ values furthermore raise the possibility of metallic

charge transport limited by macroscopic interparticle hopping transport.

Conducting organic polymers and coordination polymers also exhibit high conductivity, but the mechanism of charge transport in these materials is typically not metallic or intrinsic and relies on doped charge carriers⁶. In intrinsic molecular conductors, metallic character is always accompanied by crystalline order. The properties of NiTTFtt, which exhibits intrinsic metallic charge transport with a disordered structure, are thus highly unusual. We have therefore undertaken detailed theoretical analyses of NiTTFtt.

Theoretical analysis

Density functional theory (DFT) calculations were performed on 1D chains and 3D stacks of NiTTFtt on the basis of our structural model. Interestingly, isolated 1D chains of NiTTFtt show semi-metallic behaviour but metallic band structure forms on 3D assembly (Fig. 3a.b. respectively). Analysis of the band structure shows that metallic character arises from both π -stacking interactions within the 2D sheets (Γ to Z), as well as side-to-side S-S interactions between sheets $(\Gamma \text{ to } X)$. Similar interactions have been invoked in single-component molecular conductors⁷. We have also analysed why the metallic character of NiTTFtt is maintained with disorder by examining molecular models that can be systematically distorted (Fig. 3c). Two molecular fragments of NiTTFtt were fixed at positions that vary the slip, π -stacking and side-to-side distances as well as the interchain twist angle. The electronic structures of these models were analysed by variational two-electron reduced density matrix complete active space self-consistent field³³ and DFT calculations. This analysis demonstrates that the molecular fragments of NiTTFtt have substantial electronic overlap that is notably robust to disorder. This is illustrated by the fact that the highest occupied natural orbital-lowest unoccupied natural orbital gaps have little to no change with structural distortions (Supplementary Tables 7 and 8 and Supplementary Figs. 81 and 83). These computations explain how metallic character is preserved in amorphous NiTTFtt: periodicity is disrupted by small-scale structural disorder, but this disorder is not large enough to disrupt overlap and delocalization.

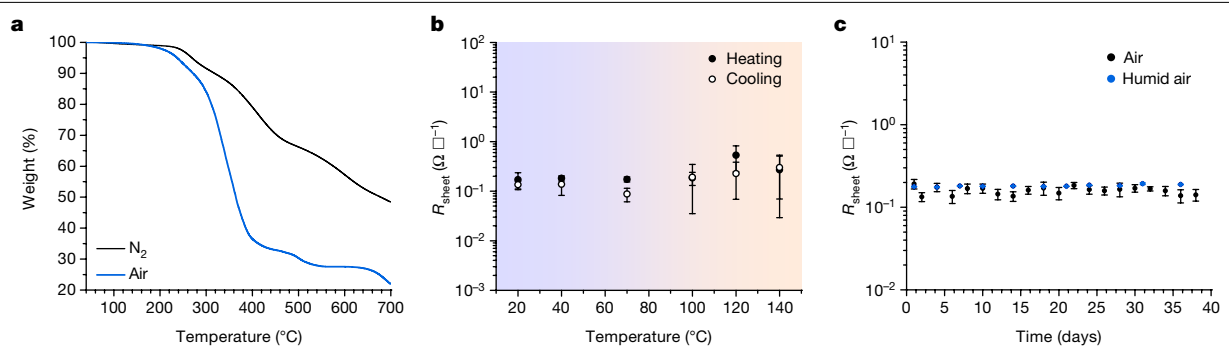


Fig. 4 | Thermal and aerobic stability of NiTTFtt. a, Thermogravimetric analysis under N2 and air. b, Sheet resistance in air on heating and cooling. c, Long-term stability of the resistance in air. Black symbols show the resistance

in ambient air and blue symbols show the resistance in 100% humid air. The data points in **b** and **c** represent the average and error bars represent standard deviations.

Thermal, aerobic and acid/base stability

The combination of structural disorder and intrinsic metallic character in NiTTFtt suggests some advantageous properties. Organic conductors, including n-type conducting polymers³⁴, coordination polymers such as Cu₃(benzenehexathiolate)³⁵ and molecular conductors, typically suffer from fast degradation when exposed to air, acid/base or heat²⁶. Metallic character in these systems arises from their crystalline structure, which can be disrupted with sufficient thermal energy (that is melting or decomposition), and exposure to air and heat leads to chemical reactions that remove charge carriers and reduce conductivity9. Although these are issues for most conducting organic materials. the disordered structure and intrinsic electronic properties of NiTTFtt suggest that it should be more robust.

Thermal stability measurements show that NiTTFtt is stable both under N₂ gas (up to 270 °C) and, notably, in air (up to 235 °C, Fig. 4a, Supplementary Fig. 62). Inspired by the stability of NiTTFtt, we monito red its sheet resistance (R_{sheet}) in air while heating and cooling between 20 and 140 °C (Fig. 4b). The high electrical conductivity of NiTTFtt is preserved even under these comparatively harsh conditions. Interestingly, pellets left in air (ambient or 100% humidity) over a month also show no conductivity loss (Fig. 4c and Supplementary Fig. 67). More remarkably, tests with acid/base demonstrate that the conductivity of NiTTFtt is relatively stable over pH 0-14 (Supplementary Figs. 70) and 71). Inspired by these observations, we generated light-emitting diode light bulb circuits with NiTTFtt, Cu foil and commercial poly(2,3-dihydrothieno-1,4-dioxin)-poly(styrenesulfonate) (Supplementary Figs. 68 and 69). The light-emitting diode brightness with NiTTFtt is similar to or better than these common conductors. These data demonstrate that the unusual combination of intrinsic metallic character with an amorphous structure in NiTTFtt imparts substantial stability for conductivity with heat, air and acid/base.

Conclusion

Organic conductors are an enormously important class of materials. Realizing conductivity in normally insulating organic materials typically requires optimization of their electronic structure through doping and their geometric structure through crystallinity. However, the requirement for doping and crystallinity imposes restrictions on composition and stability. Here we report an unusual new material, NiTTFtt, that is structurally amorphous, precluding a classical band structure. Nevertheless, detailed characterization of NiTTFtt reveals high conductivity and a metallic character. Theory shows that the presence of this metallic behaviour is enabled by overlap between the molecular units of NiTTFtt that is insensitive to structural distortions. Although an in-depth understanding of the microscopic details of charge transport in NiTTFtt requires further studies, we propose

that the metallic character arises from the conjugated NiTTFtt chains that generate an infinite π system and a negligible bandgap combined with efficient interchain orbital overlap that is robust to structural disorder. The robustness of NiTTFtt to structural disorder may be understood in the Anderson localization framework in which sufficiently wide bandwidths maintain a delocalized metallic state around the Fermi level even as structural disorder is introduced⁸ (Supplementary Fig. 88). Regardless of the exact mechanism, the juxtaposition of metallic character and disorder in NiTTFtt provides notable thermally and aerobically stable conductivity. These results demonstrate that the use of molecular units that have strong overlap, and subsequently strong electronic delocalization, can lead to metallic character even in amorphous materials.

Online content

Any methods, additional references, Nature Research reporting summaries, source data, extended data, supplementary information, acknowledgements, peer review information; details of author contributions and competing interests; and statements of data and code availability are available at https://doi.org/10.1038/s41586-022-05261-4.

- Heeger, A. J. Nobel Lecture: Semiconducting and metallic polymers: the fourth generation of polymeric materials. Rev. Mod. Phys. 73, 681-700 (2001).
- Bryce, M. R. Recent progress on conducting organic charge-transfer salts. Chem. Soc. Rev. 20, 355 (1991)
- Valade, L., de Caro, D., Faulmann, C. & Jacob, K. TTF[Ni(dmit)₂]₂: from single-crystals to thin layers, nanowires, and nanoparticles. Coord. Chem. Rev. 308, 433-444 (2016).
- Xie, L. S., Skorupskii, G. & Dincă, M. Electrically conductive metal-organic frameworks. Chem. Rev. 120, 8536-8580 (2020)
- Guo, X. & Facchetti, A. The journey of conducting polymers from discovery to application, Nat. Mater, 19, 922-928 (2020)
- Bubnova, O. et al. Semi-metallic polymers. Nat. Mater. 13, 190-194 (2014).
- Kobayashi, A., Fujiwara, E. & Kobayashi, H. Single-component molecular metals with extended-TTF dithiolate ligands. Chem. Rev. 104, 5243-5264 (2004).
- Kobayashi, Y., Terauchi, T., Sumi, S. & Matsushita, Y. Carrier generation and electronic properties of a single-component pure organic metal, Nat. Mater. 16, 109-114 (2017).
- Venkateshvaran, D. et al. Approaching disorder-free transport in high-mobility conjugated polymers. Nature 515, 384-388 (2014).
- Joo, Y., Agarkar, V., Sung, S. H., Savoje, B. M. & Boudouris, B. W. A nonconjugated radical polymer glass with high electrical conductivity. Science 359, 1391-1395 (2018).
- Plummer, J. Is metallic glass poised to come of age? Nat. Mater. 14, 553-555 (2015)
- Hirata, A. et al. Geometric frustration of icosahedron in metallic glasses. Science 341, 12 376-379 (2013).
- 13. Eisenberg, R. & Gray, H. B. Noninnocence in metal complexes: a dithiolene dawn. Inorg. Chem. 50, 9741-9751 (2011).
- McCullough, R. D. et al. Building block ligands for new molecular conductors: homobimetallic tetrathiafulvalene tetrathiolates and metal diselenolenes and ditellurolenes, J. Mater, Chem. 5, 1581 (1995).
- Xie, J. et al. Redox, transmetalation, and stacking properties of tetrathiafulvalene-2,3,6,7-tetrathiolate bridged tin, nickel, and palladium compounds. Chem. Sci. 11, 1066-1078 (2020).
- de Caro, D. et al. Metallic Thin films of TTF[Ni(dmit)₂]₂ by electrodeposition on (001)-oriented silicon substrates. Adv. Mater. 16, 835-838 (2004).
- Scott, R. A. Comparative X-ray absorption spectroscopic structural characterization of nickel metalloenzyme active sites. Phys. B Condens. Matter 158, 84-86 (1989).

- Holder, C. F. & Schaak, R. E. Tutorial on powder X-ray diffraction for characterizing nanoscale materials. ACS Nano 13, 7359-7365 (2019).
- Tanaka, H., Okano, Y., Kobayashi, H., Suzuki, W. & Kobayashi, A. A three-dimensional synthetic metallic crystal composed of single-component molecules. Science 291, 285–287 (2001).
- Vogt, T. et al. A LAXS (large sngle X-ray dcattering) and EXAFS (extended X-ray absorption fine structure) investigation of conductive amorphous Nickel tetrathiolato polymers. J. Am. Chem. Soc. 110, 1833–1840 (1988).
- Liu, Z. et al. Controlling the thermoelectric properties of organometallic coordination polymers via ligand design. Adv. Funct. Mater. 30, 2003106 (2020).
- Choy, C. L., Leung, W. P. & Ng, Y. K. Thermal conductivity of metallic glasses. J. Appl. Phys. 66, 5335–5339 (1989).
- Sun, L. et al. A microporous and naturally nanostructured thermoelectric metal-organic gramework with ultralow thermal vonductivity. *Joule* 1, 168–177 (2017).
- Craven, G. T. & Nitzan, A. Wiedemann–Franz Law for molecular hopping transport. Nano Lett. 20, 989–993 (2020).
- Dou, J. H. et al. Signature of metallic behavior in the metal-organic frameworks M₃(hexaiminobenzene)₂ (M = Ni, Cu). J. Am. Chem. Soc. 139, 13608–13611 (2017).
- Kaiser, A. B. Electronic transport properties of conducting polymers and carbon nanotubes. Reports Prog. Phys. 64, 1–49 (2001).
- Halim, J. et al. Variable range hopping and thermally activated transport in molybdenum-based MXenes. Phys. Rev. B 98, 104202 (2018).
- Lan, X. et al. Quantum dot solids showing state-resolved band-like transport. Nat. Mater. 19, 323–329 (2020).

- Kang, S. D., Dylla, M. & Snyder, G. J. Thermopower-conductivity relation for distinguishing transport mechanisms: polaron hopping in CeO₂ and band conduction in SrTiO₃. Phys. Rev. B 97, 235201 (2018).
- Heeger, A. J. Disorder-induced metal-insulator transition in conducting polymers.
 J. Supercond. 14, 261–268 (2001).
- Jiang, Y. et al. Synthesis of a copper 1,3,5-triamino-2,4,6-benzenetriol metal-organic gramework. J. Am. Chem. Soc. 142, 18346–18354 (2020).
- 32. Lee, K. et al. Metallic transport in polyaniline. Nature 441, 65-68 (2006).
- Mazziotti, D. A. Large-scale semidefinite programming for many-electron quantum mechanics. Phys. Rev. Lett. 106, 083001 (2011).
- He, T., Stolte, M. & Würthner, F. Air-stable n-channel organic single crystal field-effect transistors based on microribbons of core-chlorinated naphthalene diimide. Adv. Mater. 25, 6951–6955 (2013).
- Huang, X. et al. Superconductivity in a copper(II)-based coordination polymer with perfect Kagome structure. Angew. Chemie Int. Ed. 57, 146–150 (2018).

Publisher's note Springer Nature remains neutral with regard to jurisdictional claims in published maps and institutional affiliations.

Springer Nature or its licensor holds exclusive rights to this article under a publishing agreement with the author(s) or other rightsholder(s); author self-archiving of the accepted manuscript version of this article is solely governed by the terms of such publishing agreement and applicable law.

© The Author(s), under exclusive licence to Springer Nature Limited 2022

Methods

Synthesis

Unless otherwise noted, all synthetic manipulations were performed under an inert atmosphere of dry N_2 using a Schlenk line or a N_2 -filled MBraun UNILab glovebox. Dichloromethane (DCM) was initially dried and sparged with Ar on a solvent purification system from Pure Process Technologies and stored over 4 Å molecular sieves. Methanol (MeOH) was dried with NaOH, distilled before being transferred and then passed through activated alumina and stored over 4 Å molecular sieves in the glovebox. TTFtt(SnBu_2)_2, Fc^{BzO}BAr_4^Fand [TEA]_2[NiCl_4] were synthesized following previously reported procedures 15,36 .

NiTTFtt. TTFtt(SnBu₂)₂ (0.667 mmol, 266 mg) in 5 ml DCM was mixed with Fc^{BzO}BAr₄^F (1.33 mmol, 1.54 g) in 5 ml DCM resulting in a homogenous dark purple solution. The resulting solution was added into a 10 ml MeOH solution of [TEA]₂[NiCl₄] (2.00 mmol, 920 mg) with vigorous stirring. The mixture was stirred at 40 °C overnight. The solid product was isolated by centrifugation and washing with DCM (3×12 ml), MeOH (1×12 ml) and DCM (1×12 ml) sequentially. After being dried under vacuum at 100 °C overnight, 235 mg of NiTTFtt was isolated as a black powder (91%).

Semicrystalline NiTTFtt. TTFtt(SnBu $_2$) $_2$ (0.040 mmol, 43 mg) in 0.4 ml DCM was mixed with Fc $_4$ (0.080 mmol, 93 mg) in 0.4 ml DCM to form a homogenous dark purple solution. After mixing, 0.8 ml of this dark purple solution was added into a clean 5 ml shell vial and 2.4 ml of a 1:1 DCM:MeOH solution (by volume) and then 0.8 ml of pure MeOH were slowly layered on the DCM layer sequentially, forming three distinct layers. Finally, a 0.8 ml MeOH solution of [TEA] $_2$ [NiCl $_4$] (0.12 mmol, 55 mg) and LiCl (0.40 mmol, 17 mg, as an optional modulator) was layered on top. The shell vial was carefully capped and placed in a secondary 24 ml vial that was allowed to sit and diffuse for 5 days. The resulting black powders were collected and washed identically to the procedure for amorphous NiTTFtt described above yielding 13 mg (85%).

Pressed pellets. Pressed pellets were prepared at 800 MPa in the glove-box by using a hydraulic pellet press (TMAX-15T) and dies with different sizes (7, 8 and 12 mm round dies and 6 mm square dies). Hot pressing was carried out with an additional heated die (13 mm Across International heated die with digital controller). Before pressing, powders were ground to particle sizes below 20 μm . For hot-pressed samples, 240 mg of powder was ground with a ball mill (Spex SamplePrep 5100 Mixer miller, 440C steel balls) for 15 min (in air) and loaded into 13 mm round dies that were preheated to 150–200 °C (under N_2). During pressing the pressure was maintained for 5–20 min after stabilizing at 800 MPa. The thickness of the pressed pellets is around 100–300 μm .

Structural characterization

X-ray powder diffraction. PXRD for screening reaction conditions was performed on a SAXSLAB Ganesha equipped with a Xenocs GeniX3D Cu K α source. Samples were loaded into 0.8–1.1 mm internal diameter, 0.25 mm wall borosilicate capillaries and sealed with wax. Data reduction and integration was performed using the Saxsgui software. In addition, a Rigaku SmartLab X-ray diffractometer equipped with a HyPix3000 detector was used for measurements in either transmission or reflection modes. For transmission, both samples of amorphous and semicrystalline NiTTFtt were loaded into 1.0 mm outer diameter, 0.01 mm wall borosilicate capillaries as fine powders and sealed with wax. All measurements were carried out with Cu K α radiation (1.54186 Å). Scans were measured using a parallel beam mode selected through the attached Cross Beam Optics. The tube was energized at 44 mA and 40 kV. The data collection was completed in the SmartLab Studio II software package (v.4.4.241.0).

Synchrotron X-ray powder diffraction. Synchrotron PXRD was collected at beamline 11-BM at the Advanced Photon Source (APS) at Argonne National Laboratory. The sample of semicrystalline NiTTFtt was loaded into Cole Parmer Polyimide tubing provided by the beamline and capped with clay. The powders were rotated during the measurement at around 50 Hz. The powder patterns were measured at 295 K using a wavelength of λ = 0.458126 Å, from 0.5 to 50° 2 θ with a step size of 0.001° and a counting time of 0.1 s per step.

X-ray absorption spectroscopy. Powder samples were prepared by grinding finely with polypropylene as a binder. A Teflon washer (5.3 mm internal diameter) was sealed on one side with Kapton tape and the ground powder was then transferred to the inside of this ring before compacting with a Teflon rod and sealing the remaining face with Kapton tape. X-ray absorption near-edge spectra of Ni K-edge (8,333 eV) data were acquired at the MRCAT 10-BM beamline in transmission at APS at Argonne National Laboratory with a bending magnet source with ring energy at 7.00 GeV. Data collected were processed using the Demeter software suite³⁷ by extracting the extended X-ray absorption fine-structure oscillations $\chi(k)$ as a function of photoelectron wavenumber k. The theoretical paths were generated using FEFF6 (ref. ³⁸) and the models were done in the conventional way using the fitting program Artemis.

X-ray total scattering and paired distribution function analysis. Samples were loaded into Cole Parmer Polyimide tubing provided by the beamline and capped with clay. High-energy X-ray total scattering experiments were performed at 11-ID-B at the APS, using an X-ray wavelength of 0.2115 Å. The raw 2D data were azimuthally integrated and reduced to 1D intensity versus 2θ in GSAS-II³⁹ using CeO₂ powder for the calibration to determine sample to detector distance. The xPDF suite program⁴⁰ was used to correct and normalize the diffraction data and then Fourier transform the reduced structure factor to obtain the PDF, G(r).

Scanning electron microscope. SEM images were taken on a Carl Zeiss Merlin using the In-Lens detector in the Materials Research Science and Engineering Center at the University of Chicago. The accelerating voltage is 5.00 kV.

Composition and vibrational characterization

X-ray photoelectron spectra. X-ray photoelectron spectra were collected with the AXIS Nova spectrometer (Kratos Analytical) equipped with a monochromatic Al K α X-ray source. The Al anode was powered at 10 mA and 15 kV. The instrument work function was calibrated to give a Au $4f_{7/2}$ metallic gold binding energy of 83.95 eV. The instrument base pressure was around 1×10^{-10} Torr. The analysis area size was 0.3×0.7 mm². For calibration purposes, the binding energies were referenced to the C 1s peak at 284.8 eV. Survey spectra were collected with a step size of 1 and 160 eV pass energy.

Ultraviolet photoelectron spectra. Ultraviolet photoelectron spectroscopy were collected with the AXIS Nova spectrometer using a UV-radiation source. The high-resolution spectra were collected with a pass energy of 40 and a 0.1 eV step size. Then 7 mm cold pressed pellets were affixed to conductive carbon tape under N_2 before loading into the spectrometer.

Inductively coupled plasma-mass spectrometry/optical emission spectroscopy. Inductively coupled plasma (ICP)-mass spectrometry (MS) data was obtained with an Agilent 7700x ICP mass spectrometer and analysed using Mass Hunter v.B01.03. Solutions for ICP-MS were prepared by digesting 2 mg of material in 1 ml HNO $_3$ (trace metal grade) solution in a fume hood overnight and diluting with ultrafiltered deionized water. An Agilent 700 series spectrometer was used for ICP-optical

emission spectroscopy (ICP–OES). The sample preparation was referred to the reported procedure 41 to improve the accuracy of sulfur determination. Solutions for ICP-OES were prepared by digesting 2 mg of materials in 0.5 ml HNO $_3$ and 0.5 ml $\rm H_2O_2$ (trace metal grade) solutions in tight-sealed high-density polyethylene centrifuge tubes overnight and then diluting with ultrafiltered deionized water.

X-ray fluorescence. X-ray fluorescence measurements were performed on pressed pellets with a Rigaku NEX DE VS spectrometer under a He atmosphere.

Combustion elemental analyses. Combustion elemental analyses (C, H, N) were performed by Midwest Microlabs.

Electron paramagnetic resonance. EPR spectra were recorded on a Bruker Elexsys E500 spectrometer with a quartz finger dewar at 77K. NiTTFtt was mixed and ground with dry KBr powder into a uniform mixture (of concentration around 0.5 mg per1 g KBr). This 'solid matrix' was loaded into the EPR tube to fill about 0.1 ml volume.

Infrared spectra. Infrared spectra were recorded on a Bruker Tensor II Fourier transform infrared spectrometer with a mercury–cadmiumtelluride detector operated at 77 K. Data were processed and background corrected with OPUS software (v.7.5). Samples were prepared under N_2 by grinding solid sample with dry KBr powder, pressed as pellets and measured in air under ambient conditions.

Raman spectra. were obtained with a Horiba LabRamHR Evolution confocal microscope. A Si(111) wafer was used for calibration. The sample of a 7 mm round pressed pellet of NiTTFtt powder was excited using a 532 nm light source operating at 5% of its power and using $100 \times long$ path objective and a $600 \ mm^{-1}$ grating.

Physical characterization

Room-temperature electrical conductivity and Seebeck measurements. Room-temperature electrical conductivity and Seebeck measurements are based on a previously reported setup⁴². Gold electrical contacts (75 nm thick) were deposited onto 8 mm pressed pellets by thermal evaporation through home-made shadow masks. Four-probe conductivity measurements were performed using a custom-designed probe station in an argon-filled glovebox. Voltage and current measurements were performed using a Keithley 2400 source meter and a Keithley 6221 precision current source. The Seebeck coefficient measurements were performed on the same probe station. Two Peltier elements were placed 5 mm apart to provide the temperature difference $(\Delta T = T_H - T_C)$. Two thermocouples were used to collect the hot (T_H) and $\operatorname{cold}(T_{\mathcal{C}})$ side temperatures, and two probes were used to measure the corresponding voltage value. A minimal amount of thermally conductive silicone paste was applied to the tips of the thermocouple to ensure good thermal contact between the thermocouple and the gold pads. A delay of 200 s was used for voltage measurements to ensure that a steady-state temperature gradient and voltage (V) were reached. The Seebeck coefficient was calculated from the slope of a linear fit for the ΔV versus ΔT plot. The measurements were taken within an approximate ΔT of ± 3 K around 300 K.

Thermal conductivities. Thermal conductivities of the samples were determined through single-laser Raman thermometry using the same confocal Raman microscope discussed above on the basis of a reported method²¹. In Raman thermometry, a focused laser beam is used as a heat source whereas the temperature-dependent Raman spectra are used as a thermometer. First, the spectral positions of the Raman peaks around 495 cm⁻¹ were measured as a function of the incident absorbed laser power (λ = 532 nm). The laser power was varied by using 0.1, 1, 2.5 and 5% of the maximum power of the 532 nm light source. The individual

powers were examined with a Si power detector. The operational setup also includes a $100 \times long$ path objective and an 1,800 mm $^{-1}$ grating. Second, the shift in the spectral position of the Raman peaks is recorded as a function of temperature, which is controlled externally by a Linkam cryostat in air.

The temperature rise in the laser spot region for the case of a semi-infinite medium can be written as $\Delta T = P_{abs}/\pi R\kappa$, where P_{abs} is the laser power absorbed by the sample, R is the Gaussian spot radius and κ is the thermal conductivity of the specimen. R is calculated by using the ToptiCalc program and based on the technical information of the laser source and the lens.

 $\label{lem:polyamble-temperature electrical resistance.} A strip of double-sided polyimide tape was placed on a d.c. resistivity/Electrical Transport Option (ETO) sample puck (Quantum Design P102), which serves as an electrical insulator, and then pressed pellets with 75-nm-thick deposited gold contacts were put on the top of the tape. Then 0.015 inch outer diameter indium wires were used to bond to the gold nodes of the samples. The puck was then loaded into a physical property measurement system (Quantum Design) under a He-filled inert atmosphere. The four-point probe resistivity measurements on a 13 mm hot pressed pellet and two-point probe resistivity measurements on 8 mm cold pressed pellets were carried out in an a.c. mode with a d.c. excitation of 1 mA. The temperature-dependent resistivity and/or resistance measurements were performed from 300 K to 2 K.$

Variable-temperature Seebeck coefficients. Variable-temperature Seebeck coefficients were measured with a MMR Technologies Inc. K-20 Programmable Temperature Controller and a P-100 Programmable Seebeck Controller. A 1 mm \times 4 mm piece of a pressed pellet was gently put between the electrodes of the sample chip. Ag epoxy (Epoxy Technology H20E) was used for the connection between the sample and the electrodes. The sample chip was heated in a muffle furnace at 175 °C for 0.5 h for complete curing, before loading the chip into the sample device.

Solid-state magnetic measurements. Solid-state magnetic measurements were performed on a Quantum Design MPMS3 SQUID magnetometer. The bulk powder of the sample (36.0 mg) was suspended in an eicosane matrix in a polycarbonate capsule to prevent movement. Diamagnetic corrections for the capsule and eicosane were made by measuring temperature versus moment in triplicate for each to determine a moment per gram correction. Diamagnetic corrections for the sample itself were applied using Pascal's constants of each atom on the basis of the formula of NiC₆S₈.

Hall effect measurements. A 6×6 mm² pressed pellet ($264 \mu m$) and a double-sided polyimide tape was put on the sample puck (P102). Hall effect experiments were carried out on a physical property measurement system at 300 K. The maximum current of 5 mA was used during the test. While the magnetic field (H) was scanned between 0 and 7 T, the Hall resistance (R_{xy}) was measured from the Hall voltage (V_{Hall}) over the current (I) (R_{xy} (V_{Hall} /I)). The Hall coefficient (R_{H} = d R_{xy} /dH) was calculated on the basis of a linear fit of the R_{xy} -H plot.

UV-vis-NIR diffuse reflectance spectra. UV-vis-NIR diffuse reflectance spectra were collected on a Varian Cary 5000 spectrophotometer with powder samples loaded in a Praying Mantis air-free diffuse reflectance cell with KCl powder as the non-adsorbing matrix. The Kubelka–Munk conversion of the raw diffuse reflectance spectrum was obtained by applying the formula $F(R) = (1-R)^2/2R$, where F(R) is the Kubelka–Munk function and R is the diffuse reflectance.

UV-vis-NIR specular reflectance spectra. UV-vis-NIR specular reflectance spectra (200–2000 nm) were collected on a Shimadzu

UV-3600 Plus UV-vis-NIR spectrophotometer with a 5-degree relative specular reflectance accessory. IR specular reflectance spectra (570–8,000 cm⁻¹) were collected with 64 scans at a spectral resolution of 4 cm⁻¹ on an IR microscope (Hyperion 2000, Bruker Optics Inc.) coupled to a Fourier transform infrared spectrometer (Vertex 70. Bruker Optics Inc.) with a mid-IR glowbar source. As the rough surface of the pressed pellet causes non-specular reflectance light loss compared with mirror standards, the experiments were conducted following a reported method³¹ based on pressed pellets with a metal coating. First, a 12 mm pressed pellet of NiTTFtt was coated with a 100-nm-thick aluminium layer covering half of one of the faces and on the other face a 100-nm-thick gold layer was applied in the same way. Second, for UV-NIR reflectance spectra, we measured the relative reflectance of both the sample surface and the aluminium-coated surface separately with respect to the aluminium mirror. Finally, the absolute reflectance spectrum of NiTTFtt was obtained by dividing the sample's reflectance with that of the aluminium-coated surface. For the IR spectrum, the method is similar but, instead of aluminium, gold was used as the reference.

Stability tests

Thermogravimetric analysis. Thermogravimetric analysis was performed using a TA Instruments Discovery analyser. Approximately 2 mg of sample was loaded into a pre-tared Pt pan and measured under N_2 or air. Samples were measured from 35 °C to 700 °C using a linear temperature ramp of 10 °C min⁻¹. The decomposition temperature was defined to be the temperature at which less than 95% mass was left.

Differential scanning calorimetry. Differential scanning calorimetry analysis was performed using a TA Instruments Discovery analyser. Approximately 5 mg of sample was loaded into a pre-weighted Tzero aluminium pan and sealed with a Tzero hermetic lid with a TA Instruments press in an $\rm N_2$ -filled glovebox. Samples were measured in the ranges of –90–150 °C and 20–210 °C using a linear temperature ramp of 10 °C min $^{-1}$.

High-temperature variable-temperature resistance. A 7 mm pressed pellet (thickness, 162 μm) was symmetrically deposited with four gold nodes on the edges. The heated resistance measurements were carried out in air with a home-made setup. A polyimide flexible heater (PLM-106/10-P) was used as the heat source, and its temperature was read and controlled by a temperature controller (Digi-Sense Advanced Temperature Controller, Cole Parmer). The sample temperature was read by a thermometer (Traceable Thermocouple). The sheet resistances were measured by a Semiconductor Device Analyser (Keysight B1500A) using the van der Pauw method.

Long-termin-air resistance measurements. After the high-temperature varied-temperature resistance measurements were done, the same setup and sample were maintained in air and the resistance at room temperature was examined every 2 days. For humid air tests, another gold-deposited pellet was loaded in a water-filled zip bag and its conductivity was examined every 3–4 days.

Theoretical calculations

Band structure calculations. In these calculations, we determined the band structure and density of states for the 3D dimer, 3D monomer and 1D monomer models using DFT in Quantum espresso 43,44 . Thekineticenergy cutoff of basis plane-wave functions (100 Ry), Marzari-Vanderbilt–DeVita–Payne cold smearing 45 temperature (0.001 Ry), energy convergence threshold (1 \times 10 $^{-8}$ Ry) and k-point sampling were optimized to reduce error in the band structure. All calculations used a projector-augmented-wave pseudopotential with a Perdew–Burke–Ernzerhof functional and a nonlinear core correction from PSlibrary 46,47 .

Band paths and Brillouin zone images were generated using the XCrySDentool⁴⁸.

Molecular calculations. A bimolecular model was constructed from the NiTTFtt structure to emulate some possible interlayer interactions present in the amorphous extended structure, with the individual unit displayed in Supplementary Fig. 79. B3LYP/6-31G*DFT calculations with the GD3BJ dispersion correction were performed to find the potential energy surface of the bimolecular model, aiming to investigate the stability of the NiTTFtt coordination polymer solid with respect to structural distortions.

Data availability

All relevant data is included in the supplementary information. The raw datasets are available from the corresponding author upon request.

Code availability

The codes used in this study are available in the repository at https://github.com/damazz/NiTTFtt.

- Gill, N. S. & Nyholm, R. S. Complex halides of the transition metals. Part I. Tetrahedral nickel complexes. J. Chem. Soc. 1959, 3997–4007 (1959).
- Ravel, B. & Newville, M. ATHENA, ARTEMIS, HEPHAESTUS: data analysis for X-ray absorption spectroscopy using IFEFFIT. J. Synchrotron Radiat. 12, 537–541 (2005).
- Rehr, J. J. & Albers, R. C. Theoretical approaches to X-ray absorption fine structure. Rev. Mod. Phys. 72, 621–654 (2000).
- Toby, B. H. & Von Dreele, R. B. GSAS-II: the genesis of a modern open-source all purpose crystallography software package. J. Appl. Crystallogr. 46, 544–549 (2013).
- Yang, X., Juhas, P., Farrow, C. L. & Billinge, S. J. L. XPDFsuite: an end-to-end software solution for high throughput pair distribution function transformation, visualization and analysis. https://arxiv.org/abs/1402.3163 (2014).
- Morrison, C., Sun, H., Yao, Y., Loomis, R. A. & Buhro, W. E. Methods for the ICP-OES analysis of semiconductor materials. *Chem. Mater.* 32, 1760–1768 (2020).
- Ma, T., Dong, B. X., Grocke, G. L., Strzalka, J. & Patel, S. N. Leveraging sequential doping of semiconducting polymers to enable functionally graded materials for organic thermoelectrics. *Macromolecules* 53. 2882–2892 (2020).
- Giannozzi, P. et al. QUANTUM ESPRESSO: a modular and open-source software project for quantum simulations of materials. J. Phys. Condens. Matter 21, 395502 (2009).
- Giannozzi, P. et al. Advanced capabilities for materials modelling with Quantum ESPRESSO. J. Phys. Condens. Matter 29, 465901 (2017).
- Marzari, N., Vanderbilt, D., De Vita, A. & Payne, M. C. Thermal contraction and disordering of the Al(110) surface. Phys. Rev. Lett. 82, 3296–3299 (1999).
- Prandini, G., Marrazzo, A., Castelli, I. E., Mounet, N. & Marzari, N. Precision and efficiency in solid-state pseudopotential calculations. NPJ Comput. Mater. 4, 72 (2018).
- Lejaeghere, K. et al. Reproducibility in density functional theory calculations of solids. Science 351, aad3000 (2016).
- Kokalj, A. XCrySDen—a new program for displaying crystalline structures and electron densities. J. Mol. Graph. Model. 17, 176–179 (1999).

Acknowledgements This work was supported by the Army Research Office under grant no, W911NF-20-1-0091, D.A.M. and J.S.A. are grateful for support from the US Department of Energy (DOE), Office of Science, Office of Basic Energy Sciences, under award no. DE-SC0019215. H.C. and D.V.T., R.I. and D.A.M. thank the National Science Foundation for financial support under award nos CHE-1905290, CHE-1856684, and CHE-2155082, respectively. We thank N. Boynton and B. Ketter for assistance with Seebeck measurements, D. Laorenza and D. Freedman for assistance with diffuse reflectance spectroscopy, X. Jiang, Y. Fan, T. Luo and W. Lin for assistance with ICP-MS measurements, J.-A. Pan for assistance with ICP-OES measurements, H. Wu for assistance with the Dektak XT-S profilometer. A. Ritchhart for computational geometry optimizations, L. Wang for assistance with SEM and L. McNamara for help with EPR. We thank M. Goetz and the beamline staff, Y. Ding and K. Kucuk, for assistance with XAS measurements at the APS beamline 10-BM-A.B and L. C. Gallington for X-ray total scattering measurements at beamline APS 11-ID-B. The PDF measurements and analysis were supported as part of the Inorganometallic Catalyst Design Center, an Energy Frontier Research Center funded by the US DOE Basic Energy Sciences under award no. DE-SC0012702. This research used resources of APS and the Center for Nanoscale Materials, US DOE Office of Science User Facilities operated for the DOE Office of Science by Argonne National Laboratory under contract no. DE-AC02-06CH11357. Parts of this work were carried out at the Soft Matter Characterization Facility of the University of Chicago and with resources from the Research Computing Cluster. This work made use of the shared facilities at the University of Chicago Materials Research Science and Engineering Center, supported by National Science Foundation under award no. DMR-2011854.

Author contributions J.X. synthesized samples and performed their physical characterization. S.E. conducted band structure calculations. J-N.B. performed the molecular calculations. A.S.F performed and refined the structural determination. B.C. performed electrical measurements and gold depositions. T.M. and G.L.G. carried out the room-temperature

Seebeck and four-probe conductivity measurements. N.Z. and R.I. collected Raman and specular reflectance IR spectra, respectively. X.S. performed the Kramers-Kronig analysis. H.C. measured variable-temperature Seebeck coefficients. Z.C. and K.W.C. collected and analysed the PDF data. J.X. and J.S.A. conceived and wrote the manuscript. B.C., S.N.P., D.V.T., J.P. and D.A.M interpreted the data and wrote the manuscript.

Competing interests J.S.A and J.X. are inventors on patent application no. 17771266 submitted by the University of Chicago that covers TTFtt-based coordination complexes and materials.

Additional information

Supplementary information The online version contains supplementary material available at https://doi.org/10.1038/s41586-022-05261-4.

Correspondence and requests for materials should be addressed to John S. Anderson.

Peer review information *Nature* thanks Satoshi Horike and the other, anonymous, reviewer(s) for their contribution to the peer review of this work.

Reprints and permissions information is available at http://www.nature.com/reprints.